THE ASTRONOMICAL JOURNAL VOLUME 113, NUMBER 5 MAY 1997

ROTATION OF STARLESS BOK GLOBULES

B. D. KANE[1] AND D. P. CLEMENS
Department of Astronomy, Boston University, Boston, Massachusetts 02215
Electronic mail: bkane@pldac.plh.af.mil

Received 1996 October 1; revised 1997 February 12

ABSTRACT

Fifteen small Bok globules showing no signs of current star formation were mapped at high spatial and especially spectral resolution in the ($J=1\rightarrow0$) rotational lines of CO, ^{13}CO, and $C^{18}O$, using the 14 meter radio telescope of the Five College Radio Astronomy Observatory. Maps were made with the fifteen-element 3 mm array receiver QUARRY and the 15×1024 channel autocorrelator spectrometer FAAS. From 120 to 360 positions per globule, sampled with half-beam spacing, were observed in the ^{13}CO line, while 30 to 60 full-beam-sampled $C^{18}O$ and CO positions per globule were observed. ^{13}CO and $C^{18}O$ were observed with a velocity resolution of less than 0.007 km s^{-1} channel^{-1}; CO was observed with 0.013 km s^{-1} channel^{-1} resolution. Gaussian fitting of the emission lines was used to establish mean radial velocities and uncertainties. Each globule radial velocity distribution on the sky was fit to a plane (solid-body rotation) to yield mean velocity gradients with position, and rotation axis directions. The globules were found to be rotating at rates more than an order of magnitude faster than velocity shifts attributable to local differential Galactic rotation. For globule assumed mean distances of 600 pc, the gradients range from 0.089 km s^{-1} pc^{-1} ($\omega\sim3\times10^{-15}$ s^{-1}) to 0.950 km s^{-1} pc^{-1} ($\omega\sim3\times10^{-14}$ s^{-1}). Half show gradients less than about 0.3 km s^{-1} pc^{-1}, and half show gradients greater than about 0.6 km s^{-1} pc^{-1}, distributed in a *distinctly bimodal fashion.* Detailed examination of the globule rotation curves indicated that the kinematics of ten of fifteen globule cores are well-approximated by solid-body rotation. Differential rotation and shearing motions due to external influences (ram pressure stripping and/or bow shocks) are also seen. © *1997 American Astronomical Society.* [S0004-6256(97)03305-0]

1. INTRODUCTION

In this paper, we develop answers to the following basic questions concerning the physical nature of starless Bok globules (SBGs): Do SBGs possess bulk rotational motions? If so, what are the magnitudes, directions, and natures of the rotation? Past studies have shown that quiescent globules contain cold ($T_k\sim10$ K) gas and are centrally condensed (Rickard *et al.* 1977; Arquilla & Goldsmith 1985; Zhou *et al.* 1990; Turner *et al.* 1992; Turner 1994; Lehtinen *et al.* 1995). However, past evidence has been ambiguous as to whether SBGs possess significant systematic rotational motion and whether rotation, if present, is best characterized as solid-body or differential.

Arquilla & Goldsmith (1986) analyzed a heterogeneous sample of clouds to conclude that large Bok globules with strong rotational gradients appear to be uncommon. Only three of the six globules they studied, all with previously reported rotation, were found to possess radial velocity gradients with position, and the detected gradients were smaller than previously estimated. Two of those three globules were found to have solid-body rotation, and the third had differential rotation approximated by $\omega(r)\propto r^{-1}$. Other efforts have measured values for dark cloud rotational gradients ranging from 0.3 km s^{-1} pc^{-1} to 2.9 km s^{-1} pc^{-1} (Milman 1977; Casali *et al.* 1987; Lehtinen *et al.* 1995). All of these studies have generally lacked sufficient spatial resolution to characterize the kinematics and density structures of the innermost cores of globules.

Knowledge of the rotational motion of globules is inherently limited to the component of rotation directed along the line of sight to the observer, and thus the measured rotational gradients are lower limits to the true three-dimensional gradients. Despite this limitation, this paper presents a comprehensive study of the rotational motion of fifteen starless small Bok globules. These SBGs were mapped in the rotational transitions of CO with high spatial and spectral resolution, to establish the velocity gradients and to distinguish between bulk rotational motions and more complex shearing motions.

2. STARLESS BOK GLOBULE SAMPLE

Starless Bok globules were to be selected from a homogeneous sample that is spread across the sky, a requirement which is met by entries in the CB catalog, Clemens & Barvainis (1988). From the 190 CB globules that have no detectable *IRAS* point sources identifiable as YSOs (Yun & Clemens 1990), a subsample was chosen based upon four quiescence criteria: CO ($J=2\rightarrow1$) line strengths less than about 5 K; CO linewidths generally less than 2 km s^{-1}; *IRAS* spectral energy distributions (of the cloud bulk dust emis-

[1]Research Scholar, Phillips Laboratory (GPOB), Hanscom AFB, MA 01731.

 0004-6256/97/113(5)/1799/16/$10.00

TABLE 1. Mapping center positions for the starless Bok globule sample.

Cloud ID (1)	Right Ascension [B1950] (2)	Declination [B1950] (3)	V_{LSR}[a] [km s^{-1}] (4)
CB4 (DC)	$00^h36^m16^s$	+52°35′30″	−11.3
CB16 (L1388)	03 59 14	+56 42 40	−2.2
CB17 (L1389)	04 00 35	+56 48 30	−4.7
CB24	04 54 33	+52 11 20	4.6
CB25	04 55 07	+51 59 20	5.2
CB27 (SCHO93)	05 01 00	+32 43 20	6.9
CB67 (L31)	16 47 35	−19 02 20	4.6
CB148 (B98/L239)	18 30 12	−26 03 50	6.5
CB160/CB161 (B117/B118)	18 51 13[b]	−07 29 40[b]	12.6
CB183	19 11 06	+16 29 30	6.6
CB195 (L701)	19 32 27	+12 07 52	9.6
CB202	19 40 20	+18 45 00	18.1
CB228	20 49 59	+56 04 30	−1.7
CB246 (L1253)	23 54 12	+58 17 50	−0.5

[a]CO velocities from Clemens & Barvainis 1988.
[b]Position of CB161 from Clemens & Barvainis 1988.

sion; Clemens *et al.* 1991 [CYH]) that rise steeply toward $\lambda = 100$ μm; and optical sizes less than 4′. Of the many globules that qualified, a smaller sample of 15 SBGs was selected due to the availability of optical *V*-band CCD polarimetric images of their star fields (Clemens & Leach 1987; Clemens *et al.* 1988; Kane & Clemens 1997).

The nominal central positions of the globule gas distributions were determined from low spectral resolution maps made in CO and ^{13}CO using the 14 meter radio telescope of the Five College Radio Astronomy Observatory (FCRAO) near New Salem, Massachusetts, in 1992 December, using the fifteen-element 3 mm receiver QUARRY (*Qu*abbin *A*rray *R*eceiver) (Erickson *et al.* 1992) but before FAAS (*F*CRAO *A* array *A*utocorrelation *S*pectrometer) was installed. A summary of position and velocity information for the SBG sample is found in Table 1. Beside the CB numbers, other designations for the globules are listed. DC indicates Dickman & Clemens (1983); L for Lynds (1962); B for Barnard (1927); SCHO for Schoenberg (1964). The coordinates listed in Table 1 represent those of gas intensity peaks found in this fast mapping survey, and are sometimes offset from the coordinates in the CB catalog, which report apparent centers of optical obscuration. Note that the projected proximity of CB160 and CB161 allowed them to be mapped together, for which the adopted center position of the map coincides with the emission peak of CB161.

This fifteen-member sample compares well to the 248 CB globules as a whole. The SBGs in this work have a mean mass of 9 $M_\odot$ (Kane 1995), not statistically different from the complete CB sample value of 11 $M_\odot$ (CYH). The majority of the sample of SBGs in this work are slightly smaller than the mean CB globule size, having angular sizes of about 2′–3′. While these SBGs are slightly smaller than the typical CB globule, they are still representative of CB globule shapes, having mean ellipticities of ~2. SBGs in this work are typical of the cold, 8 K globules in the CB catalog.

After the fast mapping characterization of the sample, the detailed mapping study was undertaken. The following is a synopsis of the ^{13}CO detailed mapping observations used to deduce the kinematics of the SBG sample.

3. OBSERVATIONS

These fifteen quiescent small Bok globules were observed in the $J=1\rightarrow0$ lines of CO, ^{13}CO, and C^{18}O, at FCRAO during 1994 April, 1994 November, and 1995 January. Maps were made with the QUARRY 3 mm array receiver and the 15×1024 channel FAAS autocorrelator spectrometer. The FWHM size of the main beam at the observed line frequencies was approximately 50″.

System temperatures were typically 650 K at the ^{13}CO ($J=1\rightarrow0$) frequency. All spectra were collected by frequency switching within the spectrometer bandpass. A total of 120 to 360 positions per globule was observed with half-beam spacing, mostly over 2.5 by 3 arcmin grids. Each position was observed for an average of 60 minutes. Spectra were obtained with 2.5 MHz effective total spectrometer bandwidth per beam, providing a velocity resolution of better than 0.007 km s^{-1} channel^{-1}. After removing baselines and folding, all spectra were four-channel smoothed (to 0.028 km s^{-1}), lowering the effective rms to 0.4 K (T_A^*).

Figure 1 shows a map-like presentation of the spectra obtained toward CB4 positions which show detectable ^{13}CO emission. Note that the profiles are smooth, symmetric, and simple.

After the four-channel smoothing, the effective spectral resolution of better than 0.03 km s^{-1} channel^{-1}, when combined with the high spatial resolution (20″–25″) and overall number of spectra (one hundred or more per SBG), provides an ideal data set with which to test for very low levels of cloud rotation.

4. SOLID-BODY ROTATIONAL FITS

4.1 Gaussian Fits

After all ^{13}CO data were four-channel smoothed they were visually examined and the emission lines were judged

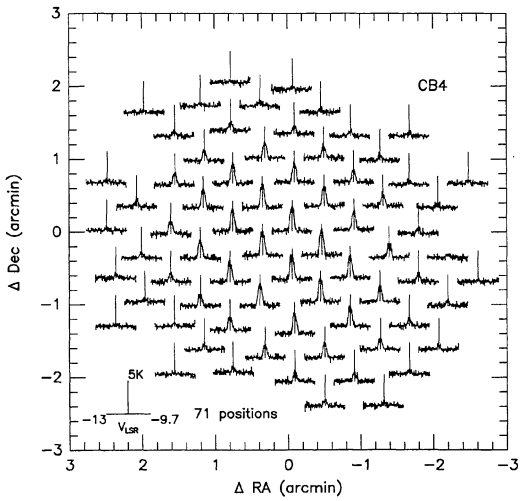

FIG. 1. ^{13}CO spectra toward CB4, arranged in a map-like distribution. The spectra are spaced about one-half beam width apart (25″), while the smoothed spectral channels are about 27 m s^{-1} wide. The spectral bandwidth displayed is about 1.25 MHz, or about 3.4 km s^{-1}, with the vertical bar indicating a mean radial velocity of −11.348 km s^{-1}, and a height representing 5 K of antenna temperature [T_A^*].

to be well described as single Gaussian-like profiles. To enable analysis, the spectral lines were then fit with single Gaussians. In all, 2278 spectra were fit; the goodness of fit was tested for each spectrum by calculating the reduced chi-square statistic (χ_ν^2). Mean χ_ν^2 values were less than 0.5 (indicating excellent fits for the globules overall), except for CB148. CB148 was observed at very low elevation, and hence its data are considerably more noisy than those of the other globules. Even so, 90% of all spectra, including those of CB148, are well fit by Gaussians. Excluding CB148, more than 99% of spectra are well fit by Gaussians.

A fit was judged successful if the 1σ uncertainty in the velocity centroid was less than about 0.013 km s^{-1}, or about one-half the smoothed velocity resolution per channel. About two-thirds of all spectra met this more stringent criterion. A summary of the 1517 successful fits is found in Table 2. For each SBG in this table, the number of positions in the map for which successful fits could be obtained is listed in column (2). The ^{13}CO line temperature at the integrated intensity peak and the offset of the peak position from the Table 1 coordinates are listed in columns (6) and (3), respectively. Also listed are the velocity centroids (4) and linewidths (5) corresponding to the Gaussian fit parameters of the peak spectrum (the first listing) and for the map average Gaussian fit parameters (second listing). Finally, the mean rms noise in the spectra and the mean χ_ν^2 of the Gaussian fit are listed in columns (7) and (8), respectively. The T_A^* in Table 2 are *uncorrected* for the main beam efficiency η (about 50%), or the coupling to these small clouds.

In a supplemental mapping effort (Kane 1995), no strong ($T_A^* > 1$ K) C^{18}O emission was found. Therefore, ^{13}CO opacities should be about 1 or smaller, and the ^{13}CO gas is expected to be a very good tracer of the bulk gas kinematics of these SBGs.

4.2 Planar Fitting

In order to measure the mean radial velocity gradients with position and the mean rotational axis directions, a simple, quick matrix inversion method was employed following Heyer (1988) and Clemens *et al.* (1992). The method works by finding the best-fitting solid-body velocity-position plane to represent the spatial distribution of observed radial velocities,

$$v_i = g_0 + g_1 x_i + g_2 y_i . \quad (1)$$

Matrix elements (positional offsets and line-center velocities) were weighted by the product of the maximum line intensity (T_A^*) and the inverse square of the velocity uncertainty:

$$w_i^2 = (T_A^*)_i (\sigma_v)_i^{-2} , \quad (2)$$

which produces a column density (i.e., mass) weighting for clouds with constant line widths. The $3 \times N$ matrix of weighted positional [(RA,Dec) $\rightarrow (-x,y)$] offsets is

$$XY = \begin{pmatrix} 1/w_1^2 & \cdots & 1/w_n^2 \\ x_1/w_1^2 & \cdots & x_n/w_n^2 \\ y_1/w_1^2 & \cdots & y_n/w_n^2 \end{pmatrix} , \quad (3)$$

and the weighted N-element velocity vector is

$$V = (v_1/w_1^2 \quad v_2/w_2^2 \cdots v_n/w_n^2) . \quad (4)$$

The 3-element gradient vector G is given by the product of V and the transpose of XY, then multiplied by the inverse of the product of XY and its transpose:

$$G = (V*(XY)^T)*[(XY)*(XY)^T]^{-1} = (V*(XY)^T)*I . \quad (5)$$

The elements of the 3-element gradient uncertainty vector, σ_G, are derived by taking the fourth-root of the diagonal elements of I:

$$\sigma_{G_i} = [I_{i,i}]^{0.25} . \quad (6)$$

The first elements of G and σ_G are the mean radial velocity $\langle v \rangle$ and its uncertainty, respectively. The mean velocities calculated in the gradient fit are within the mean errors quoted for the mean velocities in Table 2.

The second and third elements of G and σ_G are the x and y components of the velocity gradient ($\nabla v_x, \nabla v_y$) and their uncertainties, respectively. The magnitude of the total radial velocity gradient (∇v) is the geometric sum of the x and y components, while the direction of the solid-body gradient projected onto the sky, Θ_{sb}, is the arctangent of the ratio $[(-\nabla v_y)/(\nabla v_x)]$. The position angle of the rotation axis, $\Theta_{\rm rot}$, is 90° counterclockwise from the direction of the solid-body gradient. Table 3 lists in columns (2) and (5) the magnitudes of the best-fit solid-body velocity gradients and the rotation axis directions, and in columns (3) and (6) the corresponding 1σ uncertainties. The velocity gradient uncertainties amount to less than 8 m s^{-1} (about 1 channel of original spectral resolution) per 50″ two-beam sampling. Similarly, most uncertainties of the position angles of the rotation axes are less than 10° (comparable to the uncertainties of SBG background stellar polarization position angles; Kane 1995).

TABLE 2. ^{13}CO Gaussian line fit parameters.

Cloud (1)	N[a] (2)	$(\Delta\alpha,\Delta\delta)$[b] [arcmin] (3)	V_{lsr} [kms^{-1}][c] (4)	Δv (FWHM) [kms^{-1}][c] (5)	T_A^* [K] (6)	rms [K] (7)	Mean χ_ν^2 (8)
CB4	72	(−0.32,−0.33)	−11.34,−11.35(<0.01)	0.34,0.34(<0.01)	4.26	0.25	0.23
CB16	95	(−0.52,−0.36)	−2.28,−2.25(0.01)	0.68,0.56(0.01)	2.82	0.54	0.35
CB17	73	(−0.03,+0.27)	−4.66,−4.60(0.01)	0.58,0.53(0.02)	3.15	0.29	0.42
CB24	53	(+0.17,+0.00)	4.62,4.59(0.01)	0.53,0.55(0.01)	2.96	0.33	0.35
CB25	81	(−0.21,−1.06)	5.30,5.24(0.01)	0.42,0.42(0.01)	3.09	0.26	0.22
CB27	335	(−1.91,−7.82)	7.13,7.09(<0.01)	0.43,0.46(<0.01)	4.23	0.49	0.27
CB67	212	(−0.85,+0.19)	4.69,4.73(0.01)	0.63,0.65(<0.01)	4.68	0.64	0.48
CB148	97	(+0.00,+0.00)	6.56,6.58(0.01)	0.41,0.33(0.01)	4.15	1.49	2.40
CB160	32	(−2.54,+0.42)	13.10,12.89(0.05)	0.37,0.36(0.04)	1.89	0.55	0.46
CB161	10	(+0.42,−0.42)	12.54,12.64(0.06)	0.44,0.26(0.03)	2.44	0.57	0.46
CB183	89	(+0.45,+0.45)	6.55,6.53(0.01)	0.57,0.46(0.01)	2.73	0.46	0.26
CB195	100	(+0.00,+0.42)	9.64,9.64(0.01)	0.45,0.45(0.01)	3.42	0.49	0.28
CB202	56	(−0.21,+0.17)	18.11,18.07(0.01)	0.64,0.55(0.01)	2.53	0.27	0.20
CB228	92	(+0.30,+0.30)	−1.67,−1.66(0.01)	0.58,0.56(0.01)	2.24	0.46	0.30
CB246	120	(−1.23,+0.00)	−0.68,−0.58(0.01)	0.93,0.85(0.01)	2.58	0.31	0.21

[a]Number of observed positions with successful Gaussian line fitting.
[b]R.A. and DEC offsets of the peak ^{13}CO integrated intensity position from the Table 1 map center positions.
[c]Spectral line parameters listed in pairs represent values obtained via Gaussian fits to the peak emission spectrum for each cloud and via weighted means of the Gaussian fits for all cloud positions, respectively. Uncertainties in parentheses are mean errors of the weighted means.

While the SBG velocity gradients with position were characterized under the assumption of solid-body rotation, some account must be made of the quality of the resulting fits in order to quantify any deviations from the solid-body rotation assumption.

The goodness of fit was characterized by computing the r.m.s. deviation of the observed-minus-model velocity residuals. The residual at each position was defined to be the difference between the observed Gaussian-fit centroid velocity (see summary in Table 2) and the velocity predicted by the best-fit solid-body rotation model:

$$v_{sb}(x,y)=\langle v\rangle+\nabla v\ \cos(\Theta-\Theta_{sb})\sqrt{x^2+y^2}, \quad (7)$$

where $\Theta=\Theta(x,y)$ is the angle between the (x,y) position and a line of constant right ascension through the center of motion. Velocity residuals (observed-predicted) were computed at each position and then normalized by the respective measured uncertainties in the Gaussian centroid velocities. Subsequently, a weighted rms (γ) value was formed from the set of normalized residuals for each globule. The weighting for the calculation of the rms was chosen to be the peak line temperature, in accordance with the weighting for the solid-body rotation fit. The γ values are essentially the square-roots of the χ_ν^2 statistics, with temperature weighting. In column (4) of Table 3 are listed the γ (temperature-weighted rms) values of the ratio of the velocity residual to the Gaussian fitting uncertainty.

Figure 2 shows the histogram of γ values. Ideal solid-body rotation (where thermal and turbulent motions are negligible) should produce γ values significantly less than 1.0.

TABLE 3. Solid-body rotation characterizations.

	Velocity Gradient			Rotation Direction	
Cloud ID (1)	∇v [km/s/arcmin] (2)	$\sigma_{\nabla v}$ [km/s/arcmin] (3)	Residuals (γ) [normalized rms] (4)	Θ_{rot} [°E of N] (5)	$\sigma_{\Theta_{rot}}$ [°] (6)
CB4	0.016	0.002	0.45	44	7
CB16	0.044	0.005	0.97	−5	8
CB17	0.050	0.004	1.32	119	4
CB24	0.103	0.006	0.60	−142	3
CB25	0.030	0.004	0.65	144	6
CB27	0.032	0.001	0.97	−150	2
CB67	0.105	0.002	1.15	112	1
CB148	0.018	0.007	0.20	179	22
CB160	0.113	0.012	1.76	−150	7
CB161	0.171	0.015	2.05	137	5
CB183	0.019	0.005	0.45	65	13
CB195	0.033	0.003	0.45	−108	7
CB202	0.158	0.008	2.17	−86	2
CB228	0.144	0.007	0.40	−109	3
CB246	0.102	0.004	1.11	−165	2
Mean	0.076	0.006	0.98	···	6
Dispersion	0.053	0.004	0.62	···	5

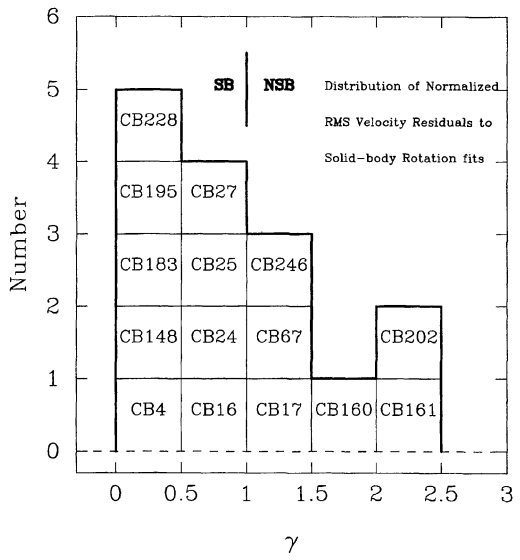

FIG. 2. Histogram of temperature-weighted rms values of the velocity residuals at each point divided by the 1σ, uncertainties in the Gaussian-fit centroid velocities at those points. These γ values measure the deviation from the model-fit solid-body rotation.

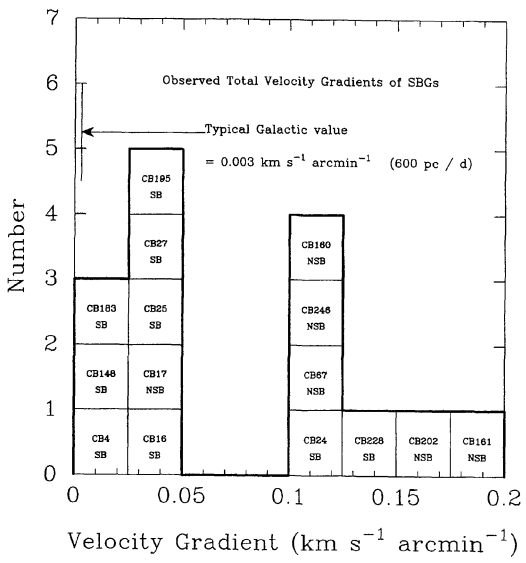

FIG. 3. Distribution of total radial velocity gradient magnitudes of the SBG sample. The typical velocity gradient due to local differential rotation of the Galaxy is marked at left and is six times smaller than the smallest measured SBG velocity gradient. "SB" denotes solid-body rotation; "NSB" applies to clouds whose rotation is strongly non-solid-body. (See Sec. *4.2* for further explanation.)

However, in the presence of thermal and turbulent motions, a globule with $\gamma=1$ possesses an rms velocity residual of only about 0.01 km s^{-1}. For $\gamma=1$ globules χ^2_ν is also roughly unity, indicating a good fit to the solid-body plane. Therefore, SBGs with γ values less than 1.0 were considered to be well modeled by solid-body rotation; this group is given the designation "SB." SBGs with γ values ranging from 1 to 3 are not well fit by solid-body rotation. Any cloud with a γ value greater than 1 was given the notation "NSB." Since the filamentary clouds show kinks which preclude the modeling of a single rotation axis, these clouds have been excluded from the detailed analysis of Sec. *5.2*.

Arquilla & Goldsmith (1986) and this work have one globule in common: CB246 (L1253). As a check of the accuracy of the matrix inversion method employed here and their sector analysis method, the position angle of the rotation axis of CB246, as calculated by Arquilla & Goldsmith, was compared and found to be only 3° different than the value in Table 3. However, they report an angular rotation speed of 4×10^{-14} s^{-1} assuming a distance of 140 pc (Snell 1981), while the angular rotation speed at 140 pc implied by the velocity gradient found in this work is $\sim 8\times10^{-14}$ s^{-1}. Our observations sample only the inner 25 arcmin^2 of CB246, which could easily be rotating twice as fast as the whole of the globule. This explanation appears to be confirmed by examining Fig. 5(a) of Arquilla & Goldsmith (1986), where spatial-velocity contours of the ^{13}CO emission profile in the globule core show a steeper velocity gradient with position than that present in the weaker, envelope emission contours.

4.3 Results

If the globules are assumed to be at a *maximum* distance of 600 pc (as for CB4; Dickman & Clemens 1983) then the *minimum* velocity gradients in physical units of km s^{-1} pc^{-1} are obtained by dividing the observed velocity-angle gradients listed in the second column of Table 3 by a factor of 0.17. The range of these minimum gradients spans 0.094 km s^{-1} pc-1 ($\omega\sim3\times10^{-15}$ s^{-1}; CB4) to 1.0 km s^{-1} pc^{-1} ($\omega\sim3\times10^{-14}$ s^{-1}; CB161). Thus, the smallest of the minimum SBG rotational gradients is a factor of six larger than the 0.015 km s^{-1} pc^{-1} ($\omega\sim5\times10^{-16}$ s^{-1}) that could be continuously supplied by local differential Galactic rotation (Clemens 1985). The mean globule rotation is a factor of 30 larger than the local Galactic value.

Figure 3 shows the distribution of observed velocity gradient magnitudes. The distribution is bimodal: about half of the SBGs possess mean radial velocity gradients less than 50 m s^{-1} arcmin^{-1}, while the other half of the SBGs have velocity gradients larger than 100 m s^{-1} arcmin^{-1}. For comparison, the gradient (3 m s^{-1} arcmin^{-1}) of a hypothetical SBG at distance 600 pc which is being spun by the local differential rotation of the Galaxy is marked to the left-hand side of the figure. If this hypothetical SBG were at 150 pc, then the apparent gradient would be four times greater, but still smaller (by 25%) than the smallest observed globule gradient. The kinematic classifications SB ("solid-body") and NSB ("non-solid-body") are also given.

To test whether the bimodality of the distribution could be an artifact of distance, we considered the case of all SBGs having the same intrinsic velocity gradients but being stratified at near (~150 pc) and far (~600 pc) distances. In this scenario, the near SBGs would have small observed velocity gradients with angular offset, while the far SBGs would have observed gradients around four times larger. However, the

SBG with the smallest observed gradient (CB4) has a rather well-determined distance of ~600 pc (Dickman & Clemens 1983); on the other hand, the large SBG CB246, appearing to rotate more than six times as fast as CB4, is estimated to be only 140 pc distant (Snell 1981). Hence, distance as the single explanation for the apparent rotational bimodality is not plausible. In a similar fashion, projection effects can be largely ruled out. Projection of true velocity gradients would tend to smooth out the distribution of measured velocity gradients; in fact, accounting for projection only strengthens the case that this is a true bimodal distribution, since the true distribution is likely to have even narrower peaks. Thus, the observed gradients should reflect a true separation into fast and slow rotators.

The subsample of globules studied by Arquilla & Goldsmith (1986) for which rotation was detected, by contrast, has a mean angular rotation speed of about 5×10^{-14} s^{-1}, larger by almost a factor of two than the most rapidly rotating globule in the SBG sample, CB161.

Of special note are the two long, filamentary clouds in the sample: the slowly rotating and bent CB27, and the rapidly rotating CB67, whose differential rotation and spatial kinks (see Figs. 10 and 11) could be classified as a "braided cylinder" geometry.

An adequate description of the sample would be that the globules separate into a group which exhibits slow, solid-body rotation (but still much faster than that which can be supplied by local Galactic differential rotation) and a group which exhibits more active kinematics not generally well-described by solid-body rotation. It is possible that in the latter group weak solid-body rotation, at levels similar to those present in the slowly rotating group, *is* present but is masked by the presence of more complex and vigorous kinematics.

5. ROTATION CURVES

Once solid-body mean radial velocity gradients and mean rotation axis directions had been measured for each SBG, the detailed natures of the departures of the rotational kinematics from the solid-body assumption were examined by constructing rotation curves.

Three types of motion might be expected for the SBGs: solid-body rotation, differential rotation, and shearing (perhaps due to ram pressure effects leading to cometary structures). Each motion will result in a different, distinct rotation curve signature. Solid-body rotation will be manifest in SBG rotation curves by velocity data which are best fit by a straight line with positional (angular) offset. Thus, in solid-body rotation, the rotation curve would closely correspond to the linear radial velocity gradient fit, for most or all of several cuts parallel to the gradient direction. Differential rotation would be present in SBGs whose rotation curves change slopes with offset from their kinematic centers, either becoming shallower with increasing offset (Keplerian motion is an example which produces such a rotation curve) or becoming steeper. Such a curve has an "S"-like shape, in which the slope usually follows the solid-body velocity gradient near the center of motion (due to the column density weighting scheme employed in the fitting) but deviates from the gradient with increasing offset from the axis of rotation. Shearing (ram pressure stripping) and turbulent flows may be responsible for rotation curves in which different cuts made parallel to the gradient directions are best fit by markedly different slopes or curves.

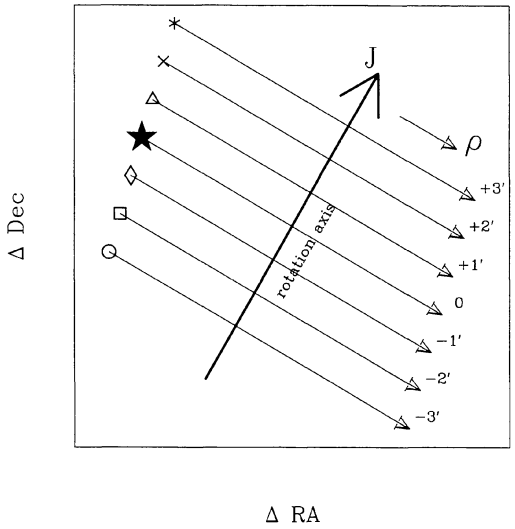

FIG. 4. A schematic view of the cuts employed in the rotation curve analyses. Equatorial offsets were transformed into a frame of reference where the coordinate increases in the direction of the angular momentum vector, $\vec{J}$ (along the rotation axis, represented by the bold line). The perpendicular cuts across this line proceed parallel to the direction of the velocity gradient, and are separated by 1′. The arrows at the right-hand ends of the cuts indicate the side selected to represent positive angular offset from the rotation axis.

Rotation curves were determined by cataloging the observed ^{13}CO mean radial velocities as functions of angular offset both perpendicular and parallel to the rotation axis and to a center of motion for each cloud. While the matrix inversion method used to measure each SBG velocity gradient does not demand knowledge of a center of motion, the derivation of a rotation curve, by definition, requires that knowledge. The rotational center of motion was identified for each cloud to be the ^{13}CO emission peak for SBGs with single spatial peaks, the major emission peak for SBGs with multiple spatial peaks, or the emission peak nearest the nominal map center for long filamentary clouds showing several peaks of similar brightness (CB27 and CB67).

Figure 4 shows in schematic form how the different cuts were obtained and provides a guide for interpreting the symbols in the figures to follow. Up to seven cuts perpendicular to the rotation axis, symmetric about the center of motion and separated by 1′ (roughly the beam size), were obtained. Each observed ^{13}CO radial velocity datum was binned into the nearest such cut, and parameterized by its distance (projected cylindrical coordinate ρ) from the rotational axis vectors passing through the centers of motion. The ρ value was chosen to be positive for offsets in the redshifted half-zone (solid-body sense; see Fig. 4), and negative in the blueshifted half-zone.

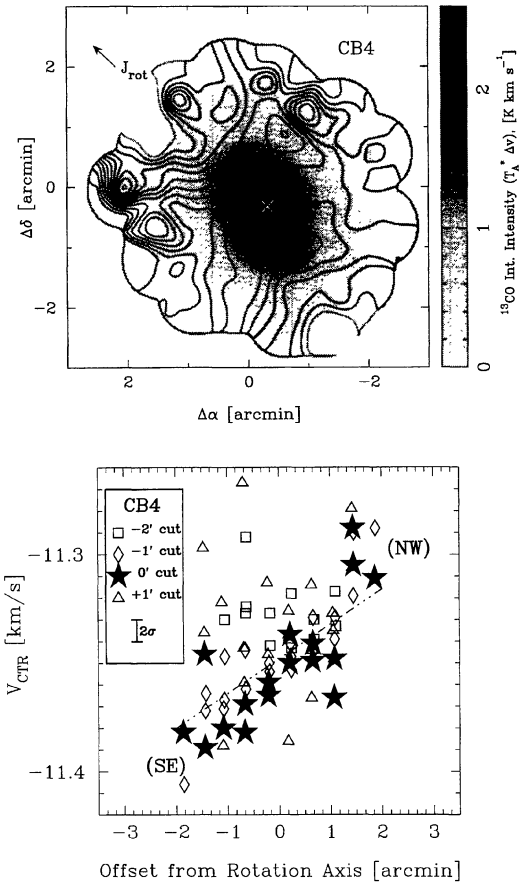

FIG. 5. *Top Panel:* Grey-scale of ^{13}CO velocity-integrated emission toward CB4, overlaid with isovelocity contours. The arrow represents the direction of the rotational axis as calculated via the velocity gradient fit. *Bottom Panel:* Rotation curve of CB4. The various symbols represent position-velocity data for several cuts normal to the rotation axis, in 1′ intervals. The approximate directions of the cut ends are noted in parentheses. The dot-dashed line represents the best-fit velocity gradient to the entire data set, weighted by ^{13}CO peak line temperature. A typical 2σ, ($\pm 1\sigma$) error bar for the velocity centroid is also shown.

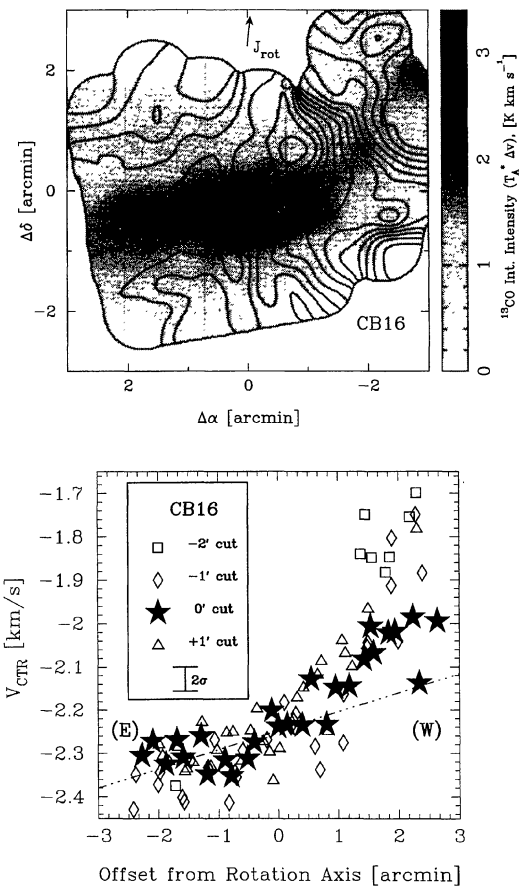

FIG. 6. *Top Panel:* Grey-scale of ^{13}CO velocity-integrated emission toward CB16, overlaid with isovelocity contours. The arrow represents the direction of the rotational axis as calculated via the velocity gradient fit. *Bottom Panel:* Rotation curve of CB16. The various symbols represent position-velocity data for several cuts normal to the rotation axis, in 1′ intervals. The approximate directions of the cut ends are noted in parentheses. The dot-dashed line represents the best-fit velocity gradient to the entire data set, weighted by ^{13}CO peak line temperature. A typical 2σ ($\pm 1\sigma$) error bar for the velocity centroid is also shown.

5.1 SBG Images and Rotation Curves

Figures 5 through 18 display the ^{13}CO data for the SBG sample. In each figure two panels are shown. The upper panel displays a gray-scale representation of the ^{13}CO integrated intensity. A "wedge" shown to the right of each top panel displays the conversion from integrated intensity, in units of $\int T_A^* dv = \mathrm{K\ km\ s^{-1}}$, to gray scale. Also in the top panel are shown contours of equal mean radial velocity. In the top panels, the refined locations of the centers of motion (from Table 2) are shown as "×" symbols.

In each lower panel, the various rotation curve cuts are shown. In those plots, the projected offsets ρ from the rotation axis are plotted versus the Gaussian-fit ^{13}CO central radial velocity for each position in the different cuts made parallel to the velocity gradient. The ^{13}CO peak line temperature-weighted solid-body rotational gradient (from Table 3) is plotted as a dot-dashed line. The most heavily weighted positions in the solid-body fit are generally contained in those cuts which pass through the centers of the SBGs. These cuts are distinguished by larger, filled stars. Data are plotted without individual error bars for the sake of clarity, but in each plot the mean 2σ, uncertainty in the line center velocity is indicated.

5.2 Classification of Rotational Kinematics

The images and rotation curve cuts were examined in order to develop classifications of the types of rotations presented by the clouds. As indicated earlier, these motions were identified as being predominantly solid-body, differential, or shearing. Clouds were also identified as being prolate (rotating about the long axis), oblate (rotating about the short axis), or significantly placed between those two extremes.

If the solid-body fit residual parameter γ was less than 1.0 (see Fig. 2) *and* the parallel rotation curve cuts for a globule were self-similar *and* showed slopes with projected offset ρ consistent with the radial velocity gradient ∇v, then the globule was judged to be engaged in *bona fide* solid-body (SB) rotation.

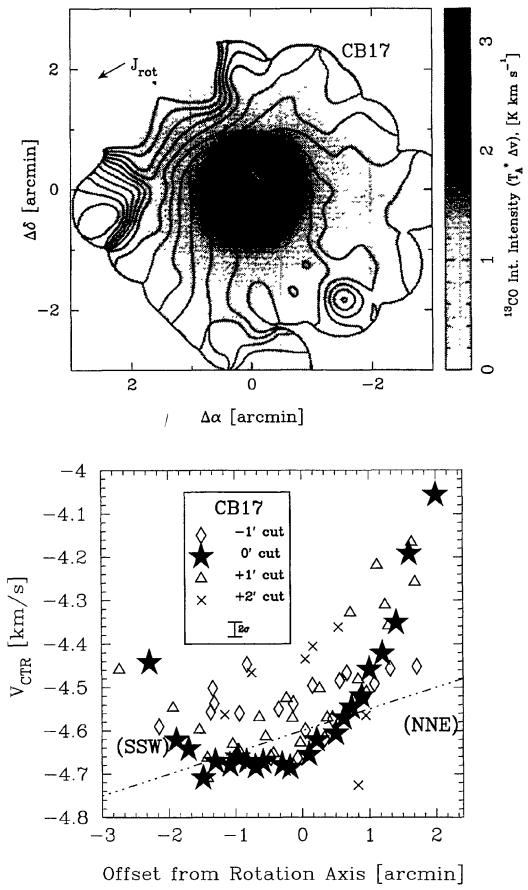

FIG. 7. *Top Panel:* Grey-scale of ^{13}CO velocity-integrated emission toward CB17, overlaid with isovelocity contours. The arrow represents the direction of the rotational axis as calculated via the velocity gradient fit. *Bottom Panel:* Rotation curve of CB17. The various symbols represent position-velocity data for several cuts normal to the rotation axis, in 1′ intervals. The approximate directions of the cut ends are noted in parentheses. The dot-dashed line represents the best-fit velocity gradient to the entire data set, weighted by ^{13}CO peak line temperature. A typical 2σ ($\pm 1\sigma$) error bar for the velocity centroid is also shown.

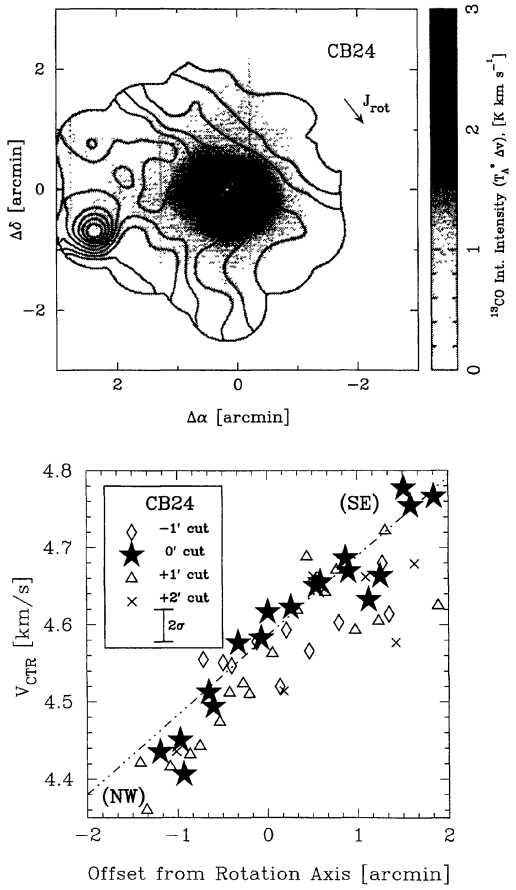

FIG. 8. *Top Panel:* Grey-scale of ^{13}CO velocity-integrated emission toward CB24, overlaid with isovelocity contours. The arrow represents the direction of the rotational axis as calculated via the velocity gradient fit. *Bottom Panel:* Rotation curve of CB24. The various symbols represent position-velocity data for several cuts normal to the rotation axis, in 1′ intervals. The approximate directions of the cut ends are noted in parentheses. The dot-dashed line represents the best-fit velocity gradient to the entire data set, weighted by ^{13}CO peak line temperature. A typical 2σ ($\pm 1\sigma$) error bar for the velocity centroid is also shown.

Second, globules with slightly higher values of γ, generally between 0.5 and 1.5, were often found to display sets of rotation curve cuts which differed from each other significantly. These globules were classified as having additional shearing motions present.

Globules showing values of γ greater than 1.0 were classified as having non-solid-body (NSB) motion. The value of 1.0 was chosen to be the cut-off between SB and NSB motion to reflect the fact that the γ value is a temperature-weighted approximation of the χ^2_ν statistic. Furthermore, upon examination of the kinematic data of CB67, which showed rotation curves containing changing slopes, CB67 was classified as differentially rotating. Differential rotation was classified as "Keplerian decay"-like (steep velocity gradient with position in the cloud core, falling to a shallower slope in the cloud periphery) and given a "K+" label in Table 4.

Finally, ram pressure stripping, bow shocks, or an anisotropic UV radiation field could impart relative momentum to gas in the periphery of a globule compared to its center. In such cases, we expect to see *symmetric* velocity deviations with offset from the globule core. As an example, the rotation curve for CB17 (Fig. 7, lower panel) seems to show a parabolic variation of line center velocity with positional offset. In the case of CB17, the parabola "opens" to redshifted velocities relative to the globule core velocity, implying that the lower density envelope of CB17 is being blown away from us, relative to the core. In the upper panel of Fig. 7, the NNE extension of a low density tail is in evidence. However, the kinematic signature of the red-shifted low-density envelope is also seen in the SSW. The conclusion is that in addition to some weak solid-body rotation of the core of CB17, of magnitude 50 m s^{-1} arcmin^{-1}, the envelope has a motion relative to the core of up to 700 m s^{-1}. Where detected, we have classified such globules as containing envelopes possessing "distinct kinematic signatures."

In order to better illustrate this supposition that shearing motions could yield parabolic-looking rotation curves, a ki-

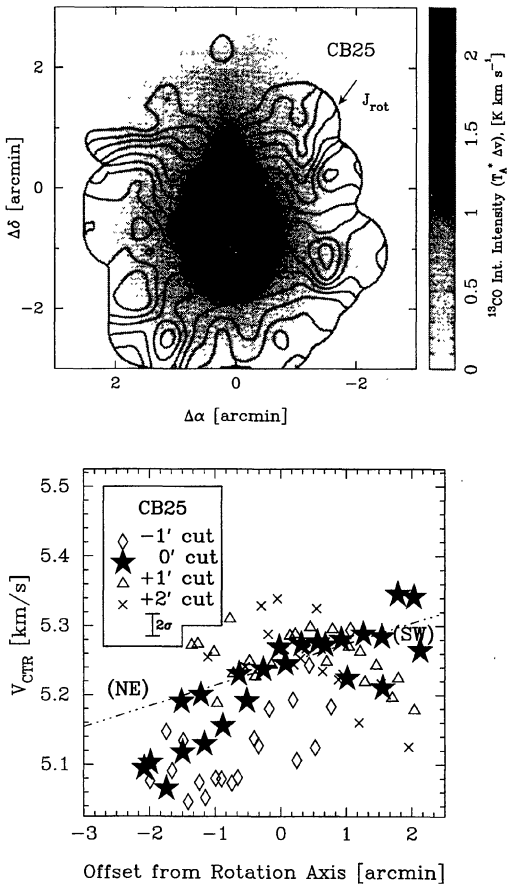

FIG. 9. *Top Panel:* Grey-scale of ^{13}CO velocity-integrated emission toward CB25, overlaid with isovelocity contours. The arrow represents the direction of the rotational axis as calculated via the velocity gradient fit. *Bottom Panel:* Rotation curve of CB25. The various symbols represent position-velocity data for several cuts normal to the rotation axis, in 1′ intervals. The approximate directions of the cut ends are noted in parentheses. The dot-dashed line represents the best-fit velocity gradient to the entire data set, weighted by ^{13}CO peak line temperature. A typical 2σ ($\pm 1\sigma$) error bar for the velocity centroid is also shown.

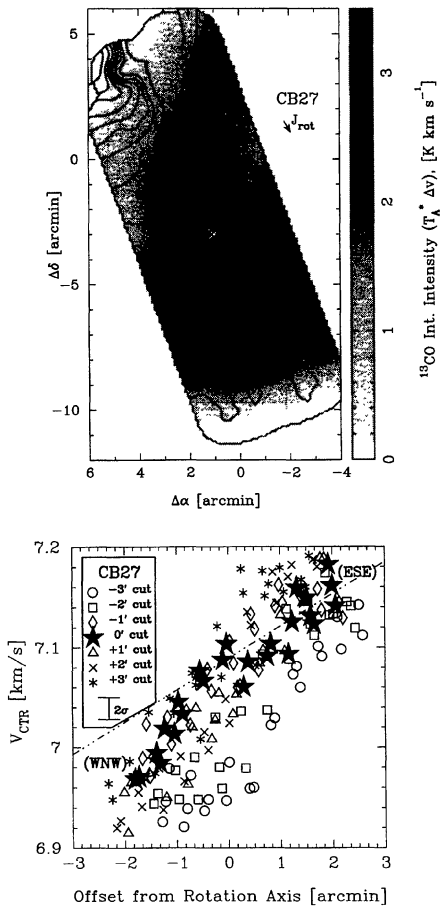

FIG. 10. *Top Panel:* Grey-scale of ^{13}CO velocity-integrated emission toward CB27, overlaid with isovelocity contours. The arrow represents the direction of the rotational axis as calculated via the velocity gradient fit. *Bottom Panel:* Rotation curve of CB27. The various symbols represent position-velocity data for several cuts normal to the rotation axis, in 1′ intervals. The approximate directions of the cut ends are noted in parentheses. The dot-dashed line represents the best-fit velocity gradient to the entire data set, weighted by ^{13}CO peak line temperature. A typical 2σ ($\pm 1\sigma$) error bar for the velocity centroid is also shown.

nematic model was constructed and tuned to mimic the CB17 behavior. The model computes emergent optically thin line profiles along an axis perpendicular to the rotation axis (the "gradient axis"). Specified in the model are the radial distributions of gas density, rotational angular velocity, and shear velocity. Along each line of sight within each volume element a Gaussian line profile is generated with a constant linewidth (no variation with radius). The model parameters were tuned to reflect parameters of the globule data sample (the gas dispersion value and spectral channel step size) and of CB17 (angular size, angular rotation rate, shear rate). Gaussian generated noise was added to the final spatial-velocity images to simulate the quality of the observed data.

Figure 19 shows a comparison of the CB17 rotation curve data with the spatial-velocity emission image computed for one set of model parameters. The CB17 data are shown as black or white stars and represent the Gaussian fitted line profile center velocities as a function of positional offset perpendicular to the rotation axis measured through the globule center (these are the same data as those shown as filled stars in the lower panel of Fig. 7). The halftones and contours display the emergent intensity from different positions along that gradient axis versus velocity. This figure demonstrates that the CB17 line profile fits are excellent matches to the line profile distributions in the model.

The two main aspects of the CB17 data which presented the strongest model constraints were the overall parabolic distribution of velocity with position, and the asymmetry represented by the steeper rise of the velocity data with positional offset for positive positional offsets (toward the NE in the upper panel of Fig. 7). In our suite of models, parabolas were generated when shear motions were included, and in particular the parabolic shape was found to depend on the power law description of the shear velocity with radius in the model. The model globule presented in Fig. 19 contains a core-halo radial structure, with volume density changing as the inverse of the radius (probably softer than in reality). The

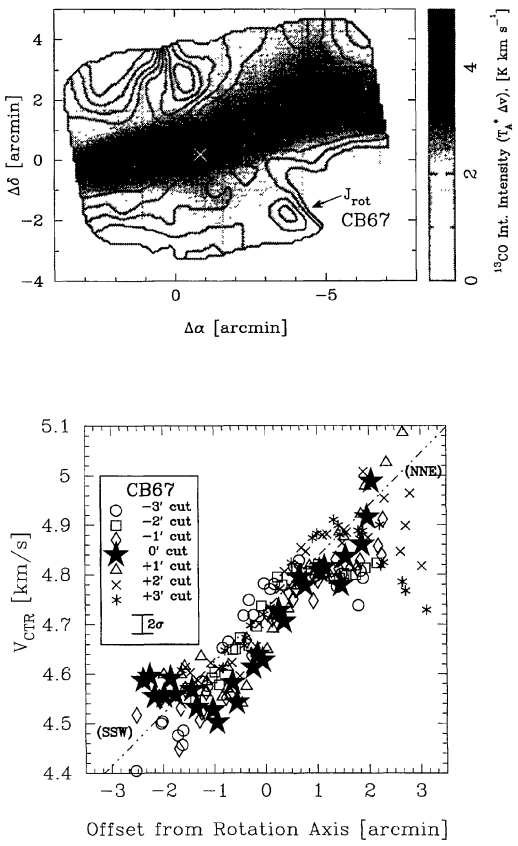

FIG. 11. *Top Panel:* Grey-scale of ^{13}CO velocity-integrated emission toward CB67, overlaid with isovelocity contours. The arrow represents the direction of the rotational axis as calculated via the velocity gradient fit. *Bottom Panel:* Rotation curve of CB67. The various symbols represent position-velocity data for several cuts normal to the rotation axis, in 1′ intervals. The approximate directions of the cut ends are noted in parentheses. The dot-dashed line represents the best-fit velocity gradient to the entire data set, weighted by ^{13}CO peak line temperature. A typical 2σ ($\pm 1\sigma$) error bar for the velocity centroid is also shown.

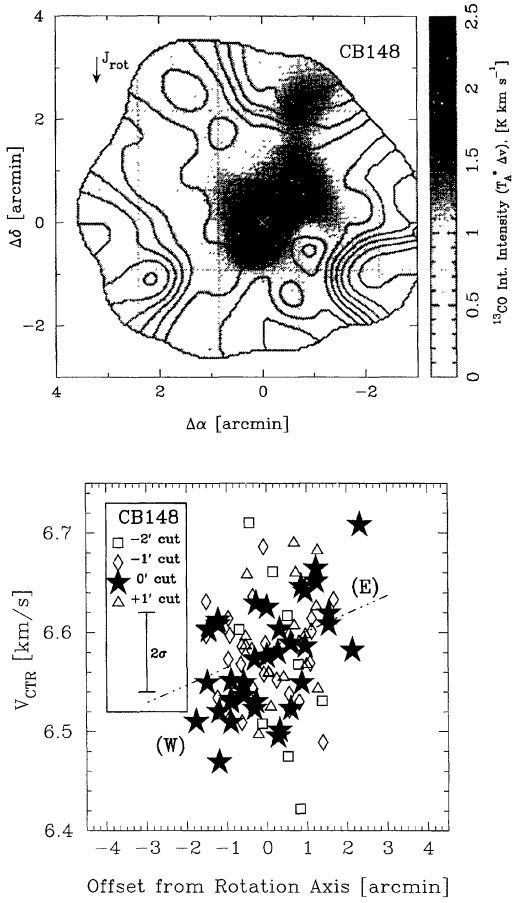

FIG. 12. *Top Panel:* Grey-scale of ^{13}CO velocity-integrated emission toward CB148, overlaid with isovelocity contours. The arrow represents the direction of the rotational axis as calculated via the velocity gradient fit. *Bottom Panel:* Rotation curve of CB148. The various symbols represent position-velocity data for several cuts normal to the rotation axis, in 1′ intervals. The approximate directions of the cut ends are noted in parentheses. The dot-dashed line represents the best-fit velocity gradient to the entire data set, weighted by ^{13}CO peak line temperature. A typical 2σ ($\pm 1\sigma$) error bar for the velocity centroid is also shown.

ratio of core to halo radii was 0.6. Shear was included as a constant velocity for all core radii then as a continuous power law of radius for the halo. Power laws with radial powers of unity tended to produce model runs of velocity with positional offset which were more linear than seen in the CB17 data, while radial powers of two produced parabolic deviations of velocity with offset. The asymmetry mentioned was found to be related to the bulk cloud rotation. In the model, once the solid-body rotation rate reported in Table 3 was included, for an assumed distance of 400 pc to CB17, the model asymmetry matched the real data.

The overall excellent match of the CB17 data to the model shown indicates that inclusion of the effects of a density distribution, solid body rotation, and shear are sufficient to accurately describe the detailed kinematics of globule core and envelope regions. Additionally, the conclusion that shear is present allows predicting the behavior seen in rotation curve cuts which do not pass through the globule cores. In the presence of shearing motions, cuts which are offset from the core (see lower panel of Fig. 7) are *expected* to be offset in velocity toward the parabola tips because those lines of sight contain higher ratios of envelope-to-core gas column density than seen in the central parts of cuts though globule centers, and the offset cuts will thereby more heavily sample the (shearing) envelope kinematics.

Table 4 lists the SBGs and a classification of their shapes, rotation rates, and dominant types of motion according to the kinematic classes listed at the beginning of this section: rotation (solid body, non-solid-body, or differential rotation), shearing, turbulent motion, and thermal motions. In addition, shearing is noted by the presence or absence of a kinematically distinct envelope (where present, the radial direction and magnitude of the motion of the envelope relative to the core is listed). Shearing may also induce turbulence on a scale too small to be directly measured. However, a statistical measure of the fit of the velocity field to the solid-body model may provide an estimate of the degree of turbulence. The unnormalized rms velocity residual is listed in Table 4, as an estimate of the magnitude of the motions in turbulent cells within the globules.

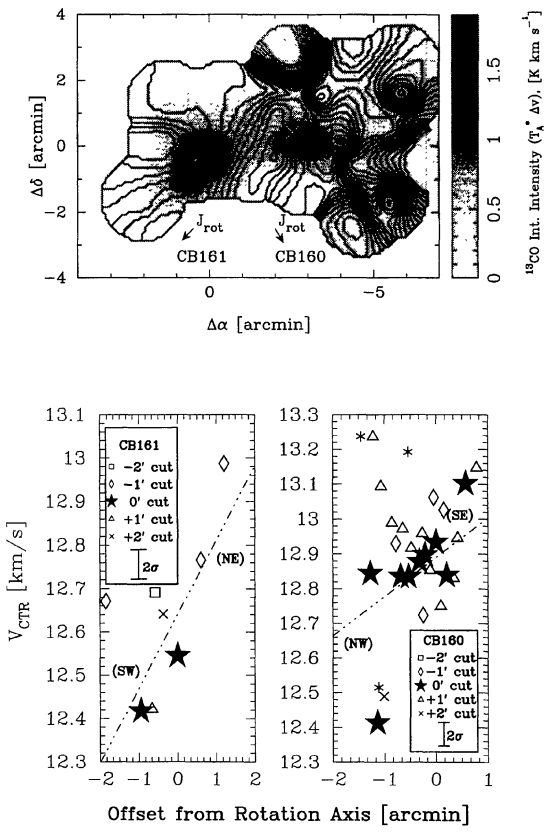

FIG. 13. *Top Panel:* Grey-scale of ^{13}CO velocity-integrated emission toward CB160 and CB161, overlaid with isovelocity contours. The arrow represents the direction of the rotational axis as calculated via the velocity gradient fit. *Bottom Panel:* Rotation curves of CB160 and CB161. The various symbols represent position-velocity data for several cuts normal to the rotation axis, in 1′ intervals. The approximate directions of the cut ends are noted in parentheses. The dot-dashed lines represent the best-fit velocity gradients to each component globule, weighted by ^{13}CO peak line temperature. A typical 2σ ($\pm 1\sigma$) error bar for the velocity centroid is also shown.

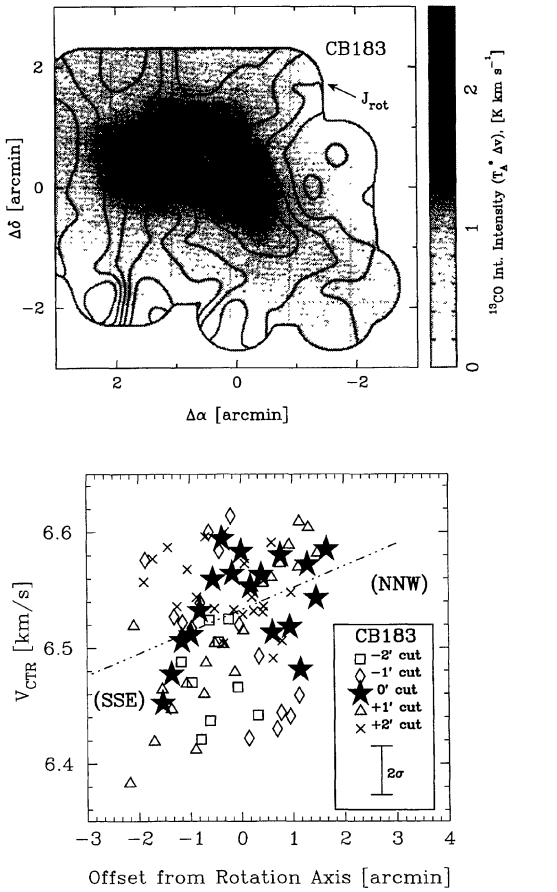

FIG. 14. *Top Panel:* Grey-scale of ^{13}CO velocity-integrated emission toward CB183, overlaid with isovelocity contours. The arrow represents the direction of the rotational axis as calculated via the velocity gradient fit. *Bottom Panel:* Rotation curve of CB183. The various symbols represent position-velocity data for several cuts normal to the rotation axis, in 1′ intervals. The approximate directions of the cut ends are noted in parentheses. The dot-dashed line represents the best-fit velocity gradient to the entire data set, weighted by ^{13}CO peak line temperature. A typical 2σ ($\pm 1\sigma$) error bar for the velocity centroid is also shown.

Clear examples of solid-body rotation are found in Figs. 5, 8, and 17 (CB4, CB24, and CB228). A good example of differential rotation is seen in Fig. 11 (CB67); the central cut shows a steep gradient in the center and a shallower gradient at either end (CB67 also exhibits a shearing or turbulent motion at the north-northeast end which steepens the gradient again). The paradigm example of a rotation curve possibly caused by shearing or turbulent flows is found in Fig. 7 (CB17).

The totals at the bottom of Table 4 indicate several things. First, 10 out of 15 clouds are prolate; all of the clouds had elongations nearly parallel or perpendicular to their axes of rotation. Second, the majority of "slow rotators" exhibit solid-body rotation, while the majority of "fast rotators" do not. Third, solid-body rotation is slightly more common than non-solid-body rotation. Finally, a large minority have kinematically distinct envelopes. These motions are probably *not* largely due to the local differential rotation of the Galaxy, but instead to large-scale differential flows (e.g., ram pressure acceleration, blast waves).

5.3 Envelopes and Tails

It is of interest to determine if the presence of an envelope is correlated with the kinematics found in the SBGs.

Here, "envelope" is defined as those parts of a cloud with low intensity emission, as compared to the much stronger cloud core emission. Thus, the degree of presence of an envelope is determined here by the relative number of low-intensity spectra obtained to the number of high-intensity spectra obtained for each cloud.

More specifically, if the logarithms of the integrated intensities at the many positions mapped for each SBG are binned into histograms, the slope of the histogram can be used as a measure of the degree of envelope presence. Figure 20 shows two examples of such histograms. The upper panel of this figure shows one example (CB183) of a globule having a histogram with a positive slope. A histogram which rises from a small number of low intensity samples to a large number of high intensity samples represents a cloud with

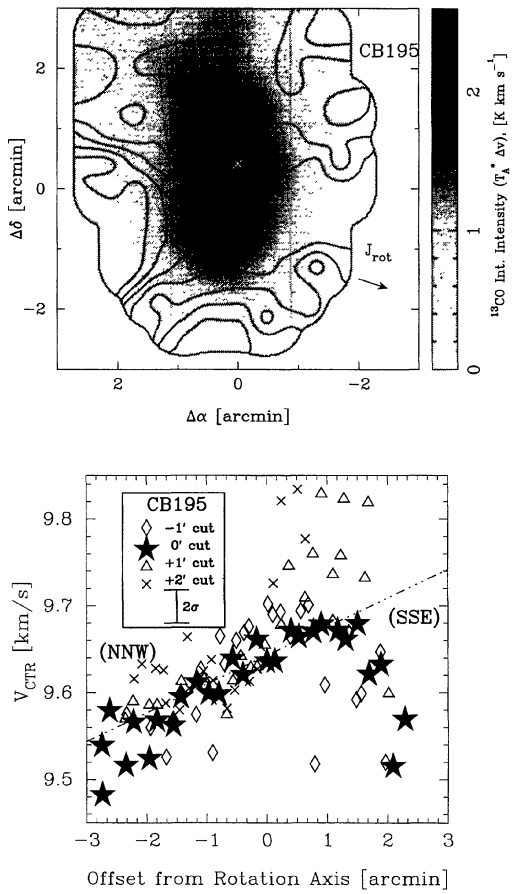

FIG. 15. *Top Panel:* Grey-scale of ^{13}CO velocity-integrated emission toward CB195, overlaid with isovelocity contours. The arrow represents the direction of the rotational axis as calculated via the velocity gradient fit. *Bottom Panel:* Rotation curve of CB195. The various symbols represent position-velocity data for several cuts normal to the rotation axis, in 1′ intervals. The approximate directions of the cut ends are noted in parentheses. The dot-dashed line represents the best-fit velocity gradient to the entire data set, weighted by ^{13}CO peak line temperature. A typical 2σ ($\pm 1\sigma$) error bar for the velocity centroid is also shown.

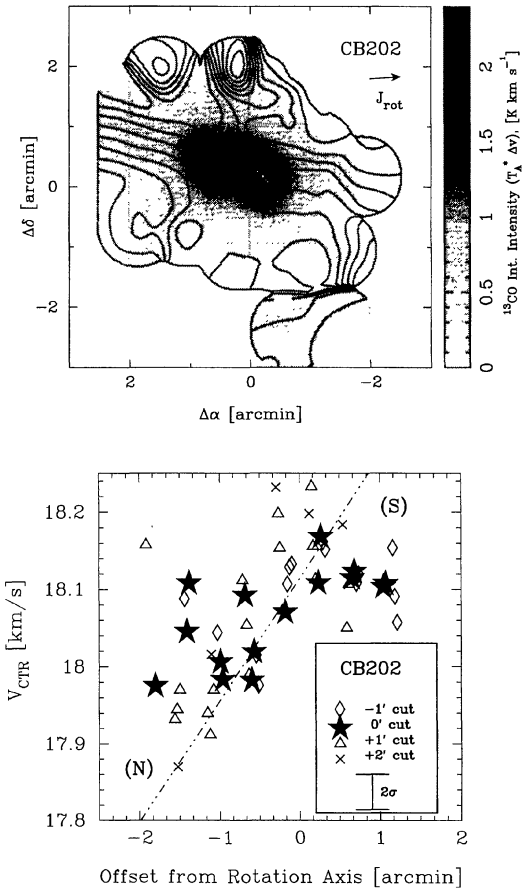

FIG. 16. *Top Panel:* Grey-scale of ^{13}CO velocity-integrated emission toward CB202, overlaid with isovelocity contours. The arrow represents the direction of the rotational axis as calculated via the velocity gradient fit. *Bottom Panel:* Rotation curve of CB202. The various symbols represent position-velocity data for several cuts normal to the rotation axis, in 1′ intervals. The approximate directions of the cut ends are noted in parentheses. The dot-dashed line represents the best-fit velocity gradient to the entire data set, weighted by ^{13}CO peak line temperature. A typical 2σ ($\pm 1\sigma$) error bar for the velocity centroid is also shown.

emission dominated by a large core, with little envelope gas. The bottom panel of Fig. 20 shows one example (CB24) of a globule with a histogram showing a flat slope, indicating a cloud which has a small, centrally condensed core and a significant envelope. By fitting for the slopes and then displaying these in another histogram, the importance of envelopes in SBGs can be evaluated.

In Fig. 21, a histogram of the slopes fit to the intensity distributions of the SBG sample is presented. Figure 21 shows that the majority of SBGs have histogram slopes clustered about 0.6. Such globules are centrally condensed into small cores and have radial intensity distributions which fall off slowly (and therefore have significant envelopes). Those SBGs with intensity distribution slopes larger than about 0.9 form a secondary population; this group is characterized by large cores and radial intensity distributions which rise quickly with increasing intensity (and therefore do not have significant envelopes). Globule envelope extents may reflect the degree of condensation of globule cores or the degree of ram pressure envelope stripping, and could be related to globule age.

5.4 Shapes and Rotational Directions

A comparison of the directions of SBG angular momentum vectors with the direction of Galactic angular momentum could lead to a better understanding of how and where SBGs have formed.

Figure 22 shows the histogram of the difference angle between the direction of the SBG rotation axes and the direction of the North Galactic Pole. This figure shows that there is no direct correlation between SBG rotation and Galactic rotation directions.

One implication of this result is that SBGs were not formed recently *in situ*, but instead in parental molecular clouds which have since been disrupted by star formation or by other forces. The creation and subsequent motions of globules have erased any signature the globules may have

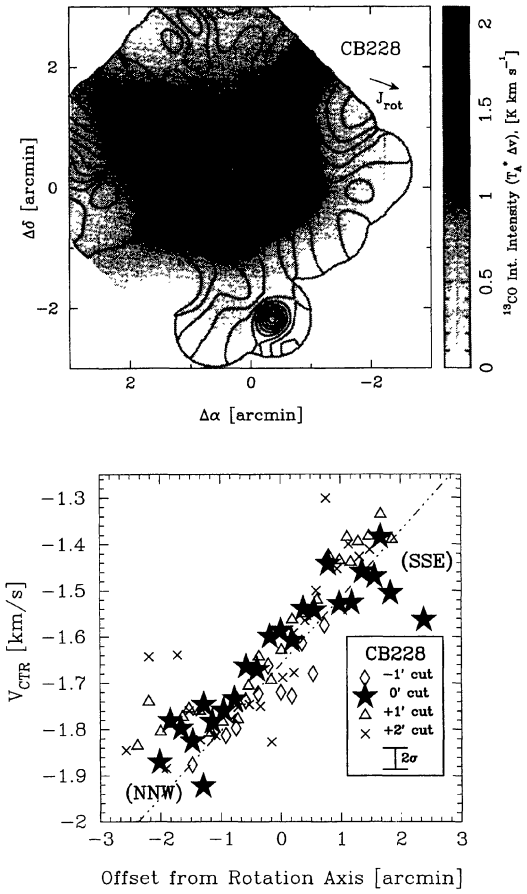

FIG. 17. *Top Panel:* Grey-scale of ^{13}CO velocity-integrated emission toward CB228, overlaid with isovelocity contours. The arrow represents the direction of the rotational axis as calculated via the velocity gradient fit. *Bottom Panel:* Rotation curve of CB228. The various symbols represent position-velocity data for several cuts normal to the rotation axis, in 1′ intervals. The approximate directions of the cut ends are noted in parentheses. The dot-dashed line represents the best-fit velocity gradient to the entire data set, weighted by ^{13}CO peak line temperature. A typical 2σ ($\pm 1\sigma$) error bar for the velocity centroid is also shown.

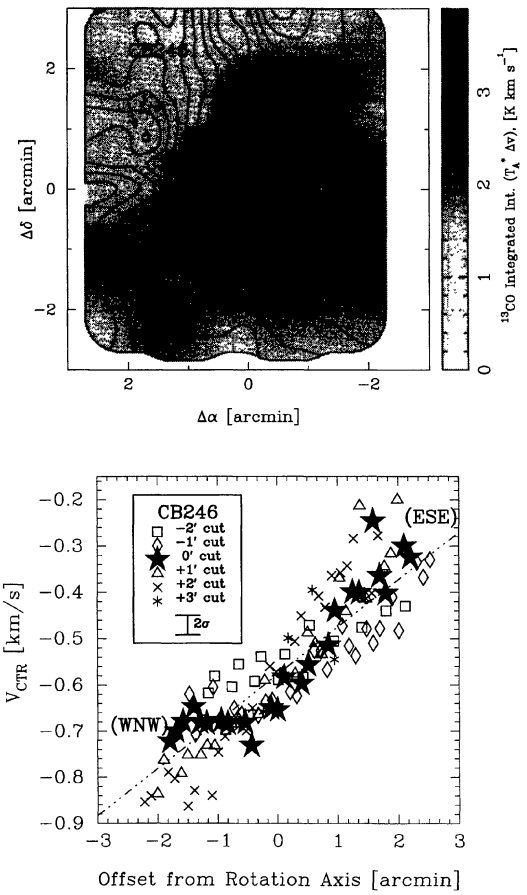

FIG. 18. *Top Panel:* Grey-scale of ^{13}CO velocity-integrated emission toward CB246, overlaid with isovelocity contours. The arrow represents the direction of the rotational axis as calculated via the velocity gradient fit. *Bottom Panel:* Rotation curve of CB246. The various symbols represent position-velocity data for several cuts normal to the rotation axis, in 1′ intervals. The approximate directions of the cut ends are noted in parentheses. The dot-dashed line represents the best-fit velocity gradient to the entire data set, weighted by ^{13}CO peak line temperature. A typical 2σ ($\pm 1\sigma$) error bar for the velocity centroid is also shown.

had of any large-scale angular momentum possessed by their parent clouds.

While SBG kinematics do not appear to be related to local Galactic dynamics, the rotational axes of the globules are all nearly parallel or perpendicular to the directions of globule elongation, as noted earlier. Ten of fifteen clouds are prolate, or elongated along their rotational axes. Of these clouds whose kinematics are well fit by solid-body rotation (the "SB" clouds), 4 of 5 are prolate. In contrast, only one of the oblate clouds is in solid-body rotation—the rest have kinematically distinct envelopes or appear to be undergoing fragmentation by showing multiple cores.

Moreover, a trend in velocity gradients of the oblate globules may be indicating a tendency to fragmentation or binary formation. CB25 and CB195, both rotating at about 30 km s^{-1} arcmin^{-1}, are elongated perpendicular to their rotation axes but do not have any obvious multiple condensation. CB16 is rotating half again as fast (about 45 km s^{-1} arcmin^{-1}) and has two major condensations. CB160 and CB161 each rotate much more rapidly than does CB16; the two cores are well separated and may represent the final products of oblate cloud fragmentation in the presence of rotation (Boss 1996).

5.5 Kinematic Decomposition

The measured ^{13}CO linewidths of the SBG sample reflect the combination of several line-broadening effects. It is of interest to assess the relative importance of the physical processes which contribute to the measured linewidths.

The excitation temperatures of ^{12}CO as measures of the kinetic temperatures of these globules (temperatures calculated in Kane 1995) lead to an estimated mean thermal CO motion of about $\Delta v_{th} = 0.08$ km s^{-1}, and a range between 0.07 and 0.09 km s^{-1}.

Several globules (e.g., CB17 [Fig. 7] and CB25 [Fig. 9]) possess rotation curves which deviate asymmetrically from solid-body rotation, thus indicating the presence of kinemati-

TABLE 4. Starless Bok globule kinematic classification.

Cloud ID (1)	Cloud Shape (2)	Cloud Rotation Rate[a] (3)	Characteristic Velocities [kms^{-1}] Rotation $D\times\nabla v$ (4)	Shear[b] (5)	Turbulent (6)	Thermal (7)	Dominant Motion (8)
CB4	prolate	Slow	0.03 (SB)	···	0.03	0.09	thermal
CB16	oblate	Slow	0.17 (SB)	0.20 (R)	0.14	0.09	shearing
CB17	prolate?	Slow	0.11 (NSB)	0.40 (R)	0.13	0.09	shearing
CB24	prolate	Fast	0.23 (SB)	···	0.12	0.07	rotation (SB)
CB25	oblate	Slow	0.07 (SB)	0.10 (B)	0.07	0.07	shear
CB27	prolate	Slow	0.24 (SB)	0.05 (B)	0.11	0.09	rotation (SB)
CB67	prolate	Fast	0.77 (K+)	···	0.26	0.09	rotation (K+)
CB148	prolate	Slow	0.05 (SB)	···	0.05	0.09	thermal
CB160	oblate	Fast	0.18 (NSB)	···	0.28	0.09	turbulent
CB161	prolate	Fast	0.33 (NSB)	···	0.20	0.09	rotation (NSB)
CB183	prolate	Slow	0.03 (SB)	0.05 (B)	0.05	0.07	thermal
CB195	oblate	Slow	0.07 (SB)	0.15 (B)	0.06	0.08	shearing
CB202	prolate	Fast	0.35 (NSB)	···	0.21	0.08	rotation (NSB)
CB228	prolate	Fast	0.28 (SB)	···	0.11	0.08	rotation (SB)
CB246	oblate?	Fast	0.60 (NSB)	···	0.20	0.08	rotation (NSB)
Totals/Means	10/15 prolate	8/15 slow	0.23(0.22) 9/15 SB	···	0.13(0.02)	0.08(0.01)	···

[a]Bimodal Slow/Fast classification according to Fig. 3.
[b]Envelope gas velocity relative (R=redshifted, B=blueshifted) to the core.

cally distinct envelopes. The deviation from solid-body rotation, due to envelope-core slipping or stripping, is estimated to be in the range of about 0.1 km s^{-1} for many of these globules; in other globules (e.g., CB4 [Fig. 5]) this motion is negligible.

The effects of shearing can best be seen in the rotation curves of the envelopes of some SBGs (e.g., CB202 [Fig. 16]), where radial velocity data points exhibit a "flayed" pattern indicating a disruption from solid-body motion. Shearing motions are estimated to range up to 0.1 km s^{-1}. Smaller scale turbulent motions, possibly initiated by large scale shearing, are estimated to range up to a few tenths of a km s^{-1} and are in most cases supersonic (see Table 4).

Finally, Table 3 shows that bulk, solid-body rotation contributes coherent velocities ranging from 0.015 to 0.15 km s^{-1} arcmin^{-1}. Since the typical SBG is 2 to 3 arcmin in diameter, rotation accounts for a motion ranging from 0.04 to 0.4 km s^{-1} across these globules. While the velocity shifts

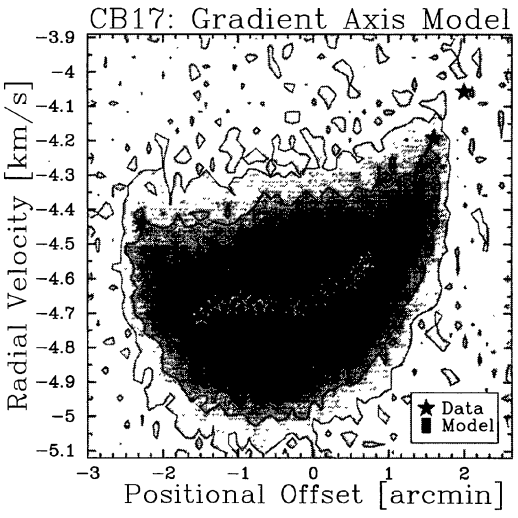

FIG. 19. Spatial-velocity diagram comparing CB17 Gaussian fit line center data with model line profiles. The data (black and white stars) are those from the central cut perpendicular to the rotation axis shown as stars in the lower panel of Fig. 7. The model (halftone and contours) shows emergent line profiles with positional offset along the same axis. In the model, the shearing component to the globule envelope velocities generates the parabolic shift of velocity with position, while the weak asymmetry of the velocity rise with offset is produced by solid body rotation of the globule.

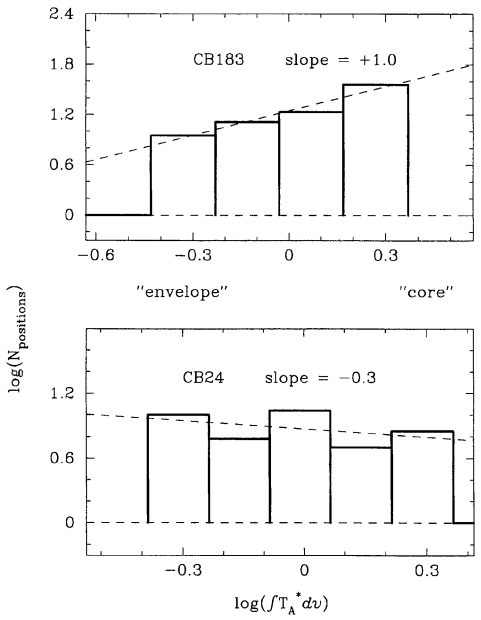

FIG. 20. Histograms of the observed occurrences of ^{13}CO integrated intensity values within the maps of two globules. *Top Panel*: log(N)–log($\int T_A^* \Delta v$) histogram of values for CB183, also showing the least-squares fit slope (dashed line). *Bottom Panel*: same as top panel, but for CB24.

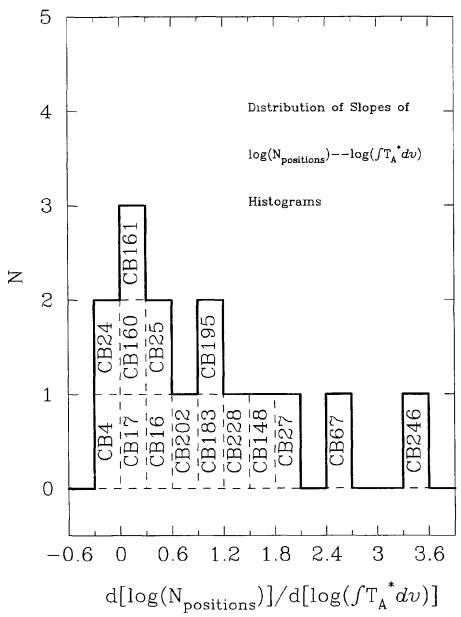

FIG. 21. Histogram of the slopes of logarithmic integrated intensity distributions.

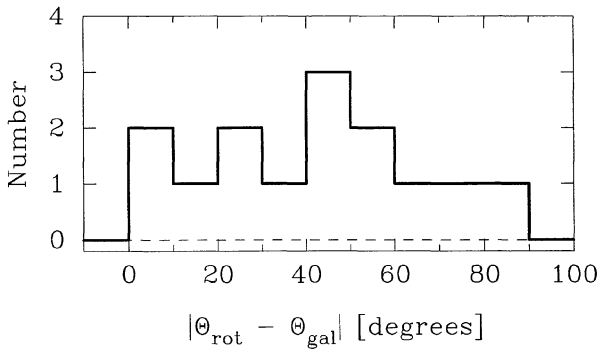

FIG. 22. Histogram of difference angles between the directions of the SBG rotation axes and the direction of the Galactic North Pole.

due to rotation in large SBGs like CB246 and in the globule sample of Arquilla & Goldsmith (1985, 1986) are greater than their linewidths, the typical SBG rotational motion is significantly less than its linewidth (and usually less than any prominent shearing or turbulent motions).

6. DISCUSSION

In the previous two sections, the kinematics of the sample of SBGs were characterized.

First, SBGs were always found to be rotating. Second, they appear to possess velocity gradients too strong to be simply driven by local differential Galactic rotation. Third, the rotational motion seems to be long lived—if it were not, most SBGs should be observed to have no detectable rotation. In spite of the ubiquity and endurance of rotation, it is nonetheless not a large reservoir of energy in SBGs. The estimated thermal energies are significantly larger, as are the energies associated with shearing motions and turbulence. However, rotation *is* large-scale and coherent and may establish a characteristic minimum specific angular momentum which can help initiate protostellar disk formation (Stahler *et al.* 1994).

The SBGs were found always to be elongated nearly parallel to their rotation axes (prolate; two-thirds of the sample), or nearly perpendicular (oblate; one-third of the sample). The kinematics of the prolate clouds are in general well-fit by solid-body rotation, while the oblate clouds may be tending toward fragmentation or binary formation.

The specific angular momentum content J/M of the globules, using J and M estimates from Kane (1995), ranges from 4×10^{-17} to 2×10^{-15} pc^2 s^{-1} and is similar to the values found for dense NH_3 cores in molecular clouds (Goodman *et al.* 1993).

For comparison, the specific angular momenta of binary protostar candidates embedded in Bok globules can be estimated by their physical separations and the kinematics of their associated molecular outflows. The angular separations are about 10″, or 0.03 pc at a distance of 600 pc (Yun & Clemens 1994) for CB52/YC1, CB54/YC1, CB60/YC1, and CB230/YC1. The estimated orbital velocities of the binaries ($\sim$1 km s^{-1} assuming a pair of 2 $M_\odot$ objects with 0.03 pc separation) suggest specific angular momenta of roughly 10^{-15} pc^2 s^{-1}, similar to the starless globules presented in this work.

Simon *et al.* (1995) made a near-infrared lunar occultation and direct imaging survey of T Tauri binary systems in the Ophiuchus and Taurus star-formation regions. The binaries observed ranged in separation from 3 AU to almost 1400 AU and on average contained about 50 times less specific angular momentum than the typical Goodman *et al.* dense core, or the Yun & Clemens embedded protostellar binaries, or the starless globules of this work.

Prosser *et al.* (1995) calculated the rotation periods of numerous main sequence stars in open clusters. The angular rotation rates they found are in the range of 10^{-5} to 10^{-6} s^{-1}. Many of these stars are of spectral type G or K, similar to the Sun in mass and radius, so that the ratio J/M for main sequence stars in their sample ranges from 10^{-22} to 10^{-20} pc^2 s^{-1}—100,000 times smaller than the typical low-mass star-forming core and 2,000 times smaller than the typical binary system (Simon *et al.* 1995).

Figure 23 summarizes the progression of specific angular momentum with size. Conservation of angular momentum would result in objects for which J/M does not vary with R. Clearly large amounts of angular momentum are being lost due to processes occurring after cloud core formation and fragmentation.

In a following paper, the radial H_2 volume density profiles of the SBG sample will be characterized. Combining the kinematic information described in this paper with density information will allow the determination of the angular momentum and energy contents of these globules. If these star-free globules contain too much angular momentum to form stable stellar systems, then some process occurring during or after the onset of star formation must be responsible for

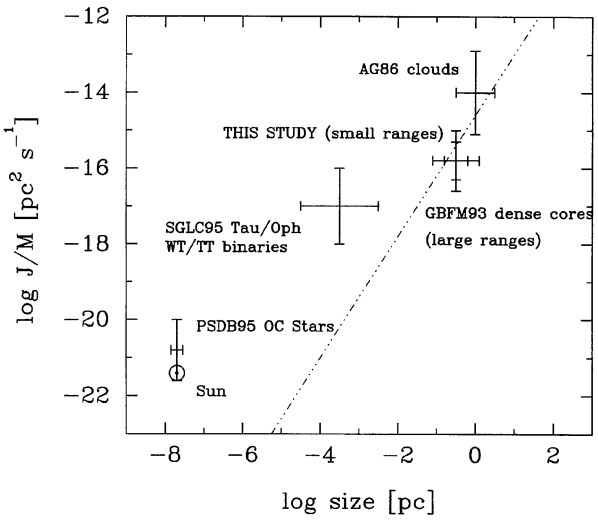

FIG. 23. Plot of specific angular momentum J/M against size for large molecular cloud cores (Arquilla & Goldsmith 1986); the starless globules in this study; dense NH_3 cores in dark cloud star formation regions (Goodman *et al.* 1993); Classical and weak-line T Tauri binary systems (Simon *et al.* 1995); late-type main sequence stars in open clusters (Prosser *et al.* 1995); and the Sun. The dashed-dotted line represents the condition of virial equilibrium ($J/M \propto R^{1.6}$).

shedding angular momentum, for example, the creation of disks or molecular outflows.

7. SUMMARY

The kinematics of a sample of starless Bok globules have been examined observationally using ^{13}CO spectroscopic mapping, and the resulting data subjected to velocity gradient and rotation curve analyses. The following points summarize the findings:

1. All the clouds in the sample show detectable bulk rotational motions.

2. There seem to be two distinct classes of starless Bok globules: "slow rotators" showing gradients of ~0.03 km s^{-1} arcmin^{-1}, and "fast rotators" showing gradients larger than ~0.1 km s^{-1} arcmin^{-1}.

3. The mean rotational rate is a factor of 25 larger than that which could be continuously supplied by the local differential rotation of the Galaxy.

4. A majority of the clouds are rotating in approximate solid-body motion. However, a significant majority exhibit signatures of shearing motions in their envelopes, which partially mask solid-body rotation in their cores.

5. Two-thirds of the clouds are prolate.

6. The one-third that are oblate may be tending toward fragmentation and/or binary formation.

7. The mean specific angular momentum J/M of the globules is similar to that of star-forming dense cores in nearby dark clouds. However, the J/M content is about 2,000 times larger than that of classical T Tauri binary systems and 100,000 times larger than that of main sequence stars.

8. The origin of cloud angular momentum remains an open question, but is likely connected to turbulence and star-formation events in larger parent molecular clouds.

This research leading to this paper was funded by NSF Grant AST 92-21194 to D. P. C., as part of the Ph. D. dissertation work by B. D. K. The Five College Radio Astronomy Observatory is funded under National Science Foundation award AST 94-20159 and is operated with permission of the Metropolitan District Commission of the Commonwealth of Massachusetts. The referee, as well as Thomas Bania, James Jackson, and Kenneth Janes, all of Boston University, and Dr. Frank Clark of Phillips Laboratory provided useful commentary. The authors thank the staff of FCRAO for their hospitality and expertise.

REFERENCES

Arquilla, R., & Goldsmith, P. F. 1985, ApJ, 297, 436
Arquilla, R., & Goldsmith, P. F. 1986, ApJ, 303, 356
Barnard, E. E. 1927, A Photographic Atlas of Selected Regions of the Milky Way. II. Charts and Tables (Carnegie Inst. Washington Pub. No. 247)
Boss, A. 1996, ApJ, 468, 231
Casali, M. M., & Edgar, M. L. 1987, MNRAS, 225, 481
Clemens, D. P. 1985, ApJ, 295, 422
Clemens, D. P., & Leach, R. W. 1987, Opt. Eng. , 29, 923
Clemens, D. P., & Barvainis, R. 1988, ApJS, 68, 257
Clemens, D. P., Leach, R. W., & Barvainis, R. 1988, in Molecular Clouds in the Milky Way and External Galaxies, edited by R. L. Dickman, R. L. Snell, and J. S. Young (Springer, New York), p. 124
Clemens, D. P., Yun, J. L., & Heyer, M. H. 1991, ApJS, 75, 877 (CYH)
Clemens, D. P., Dickman, R. L., & Ciardi, D. R. 1992, AJ, 104, 2165
Dickman, R. L., & Clemens, D. P. 1983, ApJ, 271, 143
Erickson, N. R., Goldsmith, P. F., Novak, G., Grosslein, R. M., Viscuso, P. J., Erickson, R. B., & Predmore, C. R. 1992, IEEE Trans. Microwave Theory Tech., 40, 1
Goodman, A. A., Benson, P. J., Fuller, G. A., & Myers, P. C. 1993, ApJ, 406, 528
Heyer, M. H. 1988, ApJ, 359, 363
Kane, B. D. 1995, Ph.D. Dissertation, Boston University
Kane, B. D., & Clemens, D. P. 1997, in preparation
Lehtinen, K., Matilla, L., Schnur, G. F. O., & Prusti, J. 1995, A&A, 295, 487
Lynds, B. T. 1962, ApJS, 7, 1
Milman, A. S. 1977, ApJ, 211, 128
Prosser, C. F., *et al.* 1995, PASP, 107, 211
Rickard, L. J., Palmer, P., Bulh, D., & Zuckerman, B. 1977, ApJ, 213, 654
Schoenberg, E. 1964, Bayerische Akad. Wiss., 5 (No. 26), 5
Simon, M., *et al.* 1995, ApJ, 443, 625
Snell, R. L. 1981, ApJS, 45, 121
Stahler, S. W., Korycansky, D. G., Brothers, M. J., & Touma, J. 1994, ApJ, 431, 341
Turner, B. E., Xu, L., & Rickard, L. 1992, ApJ, 391, 158
Turner, B. E. 1994, ApJ, 420, 661
Yun, J. L., & Clemens, D. P. 1990, ApJ, 365, L73
Yun, J. L., & Clemens, D. P. 1994, AJ, 108, 612
Zhou, S., Evans, N. J., & Butner, H. M. 1990, ApJ, 363, 168